Evolution of Dendritic Austenite in Parallel With Eutectic in Compacted Graphite Iron Under Three Cooling Conditions

BJÖRN DOMEIJ, JESSICA ELFSBERG, and ATTILA DIÓSZEGI

Shrinkage defects are common problems in industrially produced metal cast components. Local density changes occur during freezing, which demand material transport between parts of the casting, often involving flow of liquid through partially solid regions. Cast alloys typically freeze with a dendritic morphology, which large interface against the liquid restricts liquid flow. Recent research also indicates that this dendritic structure has an impact on the mechanical properties of the final material. For these reasons it is important to understand and predict the evolution of this structure through the solidification of cast alloys. In this work, the evolution of the dendritic austenite structure is investigated in a near-eutectic compacted graphite iron solidified under three different cooling conditions. The solidification was interrupted by water quenching, enabling characterization of the dendritic austenite structure at different stages of solidification. Higher cooling rate was found to promote a more coherent dendritic austenite structure which constituted a larger volume fraction. In parallel with growth of the eutectic, the amount of dendritic austenite in extra-eutectic regions continued to rise. This rise was associated with both tip growth of new dendrites and with growth by thickening of existing dendrites.

I. INTRODUCTION

MOST pure metals are denser in their solid state than when liquid, meaning their freezing involves contraction. The density of liquid and solid phases also tends to increase as they cool. Consequently, one of the central challenges of metal casting is to make sure material is adequately transported to shrinking regions. Failure to do so may lead to a variety of casting defects, such as the formation of pores inside the casting or distortion of its geometry. Common cast alloys are designed to reduce the shrinkage tendency by addition of an element which precipitates as a phase which has lower density than liquid, such as diamond cubic silicon (Si) in Al–Si based cast alloys and graphite in cast irons. In cast alloys, the metal typically solidifies dendritically, which plays an important role to their solidification characteristics. The large surface area of the structure against the liquid may severely restrict feeding. The dendritic structure also imposes spatial constraints on later solidified regions in which secondary phases grow, pores develop and alloying elements segregate.[1–4]

In this work, research on dendrites in cast alloys is reviewed, followed by a more focused review on dendritic austenite in cast irons. Results of recent experimental work is then presented, with aim to clarify the evolution of dendritic austenite in near eutectic compacted graphite iron. The evolution of the volume fraction and surface area of the dendritic structure is measured quantitatively using metallography and is compared to a recently reported isothermal model.[5]

A. Review on Dendrites in Cast Alloys

Darcy's law approximates the flow of liquid through porous media as proportional to the pressure gradient, where the proportionality constant is determined by a combination of the viscosity of the liquid and the permeability of the porous medium. Research on Al–Cu alloys and a Ni based alloy has shown that, based on the Kozeny–Carman equation,[6,7] the permeability of a variety of dendritic structures can be described with reasonable accuracy as a function of its volume fraction V_V^S and the surface area of its interface against the liquid per unit volume $S_V^{S/L}$,[8–11] given that the morphological

BJÖRN DOMEIJ is with the Department of Materials and Manufacturing, Jönköping University, Gjuterigatan 5, 551 11 Jönköping, Sweden. Contact e-mail: bjorn.domeij@ju.se JESSICA ELFSBERG is with the Scania CV AB, Materials Technology, 151 87, Södertälje, Sweden. ATTILA DIÓSZEGI is with the Department of Materials and Manufacturing, Jönköping University, Gjuterigatan 5, 551 11 Jönköping, Sweden.

changes over time are taken into account. Improved agreement has been achieved using a composite permeability considering both intra- and extra-dendritic flow.[8,12] Modelling of the anisotropic permeability over columnar zones has also been attempted.[13]

Aside from the restriction of liquid flow, the characteristics of the dendritic structure have also been found to correlate with the mechanical behavior of cast alloys. The average distance between secondary dendrite arms has been associated with the tensile properties of Al alloys.[14–16] A similar relation has been found for chilled cast iron.[17] Recent research also indicates that the tensile strength of hypoeutectic lamellar graphite iron (LGI) and compacted graphite iron (CGI) relates to the volume and surface area of the space constrained by the dendritic primary phase.[18–20]

For these reasons it is highly relevant to be able to predict the evolution and final shape of the dendritic structure in cast alloys, particularly with respect to its volume fraction and surface area.

The evolution of the dendritic structure through the solidification interval can be understood roughly as a combination of growth and coarsening.

An initial dendrite structure arise through tip growth and branching under the local and momentary conditions at the solidification front.[21,22] Upon further cooling, dendrite arms may continue to grow in diameter, here referred to as thickening.[23]

Aside from growth, the dendritic structure also undergoes morphological changes as long as it is in contact with liquid, driven by an excess of free energy associated with the solid–liquid interface, here referred to as coarsening.[24–28] Similar to growth by thickening, the coarsening process also contributes to an increase of the average diameter of dendrite arms, but does so at the expense of the diameter and number of smaller arms. In other words, dendrite coarsening is not dependent on cooling nor of increase of the volume fraction of solid.

Evidence from Al–Cu alloys suggests that the initial dendrite structure depends on complex interactions between tip velocity, tip radius, thermal gradient, chemical composition and the anisotropy of the surface energy of the crystal.[29] However, it has been noted that, for a given alloy, an empirical relationship with the duration of solid–liquid contact can be sufficient to approximate the average spacing between secondary arms.[30]

The coarsening process is driven by excess free energy related to the solid–liquid interface. Variations in local mean curvature over the interface drives diffusion of solute through the melt.[26–28] Low curvature regions of the interface grow by remelting of high curvature regions, leading to an overall reduction of curvature, interfacial surface area and free energy in the system.[26–28] Under isothermal conditions and constant volume fraction of solid, several characteristic length scales of the structure have been found to evolve approximately in proportion to the cube root of time $t^{1/3}$.[26–28]

B. *Review on Dendrites in Cast Irons*

A material class in which the dendritic structure has been given scarce attention is cast irons. The reason appears to be a combination of the difficulties of studying the structure and lack of understanding about its irrelevance to the production and performance of the cast material.

In hypoeutectic LGI, the evolution of the dendritic austenite through solidification has been studied at various cooling rates by interrupting the relatively slow solidification by quenching. The inverse of the specific surface area between the dendritic austenite and liquid $S_V^{D/L^{-1}}$ has been found to increase approximately in proportion to the cube root of time $t^{1/3}$.[31] In continuation of the work, the volume fraction of dendritic primary austenite was found to increase from about 0.35 at 1200 °C to about 0.42 °C at 1150 °C, with no apparent relation to cooling rate (0.04 to 0.14 K/s).[32] The volume fraction of dendritic austenite has also been measured ahead of the eutectic solidification front in Fe-C LGI quenched after partial solidification under directional cooling.[33,34] These measurements were in fair agreement with the lever-rule based on the Fe-C equilibrium phase diagram. Furthermore, the thickness and spacing of dendrite arms was found to increase throughout solidification.

Dendritic austenite has also been studied in as-cast irons based on the micro-segregation patterns of Si the structure leaves behind.[2,35,36] Using this color etching technique the volume fraction of austenite constraining the eutectic was found to be rather constant for cooling rates ranging from 0.06 to 1.2 K/s.[37] However, the volume fraction shows strong dependence on the composition, ranging from around 0.6 for a considerably hypoeutectic composition to around 0.3 for near-eutectic composition.

Considerable amounts of dendritic austenite have also been observed by many authors in near-eutectic and hypereutectic cast irons.[35,38–40] This is often attributed to poor coupling between the graphite and austenite phases, which has been clarified using the concept of coupled zone.[38,41–44]

The coarsening of dendritic austenite in hypoeutectic LGI has also been studied under isothermal conditions at temperatures between the equilibrium eutectic temperature and the temperature where primary austenite grains reach coherence for durations up to 96 hours.[5] The $S_V^{D/L^{-1}}$ was measured and shown to increase approximately in proportion to $t^{1/3}$, however with larger scatter for longer times.[5] Approximations of the slopes of the relation based on plots published for hypoeutectic LGI under isothermal conditions[5] and solidification[31] indicate that $S_V^{D/L^{-1}}$ rises at higher rate during solidification.

The ratio between the volume of dendritic austenite and surface area against the liquid has been defined as its modulus of dendrites $M^D = V_V^D / S_V^{D/L}$.[45] Researchers have argued that this parameter is a useful measure of coarseness, because it is larger for structure which

Table I. Chemical Composition of the Source SGI Material Measured Using Arc-Spark OES and Combustion Analysis

Method	CE	C	Si	Mn	P	S	Cu	Sn	Mg
Arc spark OES	4.22	3.74	1.88	0.64	0.004	0.012	0.80	0.14	0.06
Combustion	4.23	3.76							

The carbon equivalent (CE) was calculated using the formula $C + 1/3(S + P)$.

carries less surface area and is well-defined for any morphology. Moreover, under isothermal conditions M^D has been reported to be relatively insensitive to variations in V_V^D, morphological changes and dendrite fragmentation, resulting in a more reliable relation to $t^{1/3}$ than $S_V^{D/L}$.[5]

Recently, the evolution of the dendritic austenite has been characterized in a similar way in a slightly hypoeutectic CGI[46] and spheroidal graphite iron (SGI)[47] for isothermal durations of up to 90 minutes. The results indicate that the slope of the relation between M^D and $t^{1/3}$ is similar for LGI, CGI and SGI.

The evolution of the dendritic austenite in LGI, CGI and SGI appears to be rather predictable under isothermal conditions above the eutectic temperature. However, its evolution through solidification is both more relevant and less understood. Moreover, most studies have focused on the evolution of the dendritic structure above eutectic temperatures in hypoeutectic cast irons. It is less understood how it develops in parallel with growth of the eutectic.

II. EXPERIMENTAL

This study employs a remelting technique to transform a source SGI material into a CGI material.[40,48] Since this investigation concerns the remelted material, details about production of the source material are brief.

A. Source Material

The source SGI material melt was produced from pig iron, steel scrap and alloying using an induction furnace in a batch of near 500 kg. Spheroidization treatment of the melt was applied using the sandwich method. Dross was removed and the melt was poured into three 3D-printed furan sand molds, with in-stream addition of ferrosilicon inoculant.

The chemical composition of the material, displayed in Table I, was measured using an arc-spark optical emission spectrometer according to ASTM E1999-2011 on a rapidly solidified sample produced seconds before pouring the molds. The table includes an additional measurement of carbon performed on an as-cast sample using a LECO CS744: an instrument which analyses gaseous combustion products using IR absorption. The carbon equivalent (wt pct C + 1/3(wt pct S + wt pct P)) presented in the table suggests that the material has a near-eutectic composition, which is typical for commercial CGI.

The mold design includes a 5×5 grid of vertical cylindrical cavities, with open tops and the bottoms connected to a gating system. A sprue connects the gating system to a pouring cup located on top of the mold.

After the casting process, the gating system was removed, and the cylinders were machined into smaller cylindrical pieces using a lathe. The diameter of the machined cylinders varied between 37.4 mm and 38.6 mm. The weight was controlled between 399.4 and 400.5 g by adjusting the cylinder length to between 47.5 and 53.1 mm. These cylinders of SGI were then remelted and transformed into CGI according to the procedure which is described next.

B. Remelting Procedure

The remelting procedure employed in this work has been described in detail in previous publications.[40,48] In essence, the material is exposed to a heating cycle in an inert atmosphere during which it melts and the Mg-based spheroidization treatment (promotes spheroidal graphite morphology) slowly fades. With an appropriate choice of holding time, the metal subsequently solidifies as CGI.

The experimental setup shown schematically in Figure 1 is based on a vertical tube electrical resistance furnace which includes a programmable temperature control unit. One by one, the machined SGI cylinders were placed in an alumina crucible with an inner diameter between 40.0 and 41.4 mm. The crucible was placed inside the furnace on a stack of graphite cylinders at the height of the controlled temperature zone. The thermocouple which feeds temperature data to the control unit is located outside the ceramic pipe running through the furnace, which leads to some disagreement between the controlled furnace temperature and the temperature of the metal in the crucible. During the heating cycle, Ar gas with a minimum purity of 99.999 vol. pct was introduced into the furnace from the bottom at a rate of 5 L per minute. The lid at the top of the ceramic pipe includes holes for venting of excess gases.

The furnace was programmed to ramp up the temperature from 20 to 1450 °C over the course of 90 minutes. A holding time of 60 minutes was then imposed, which had been proven sufficient for the transformation of a similar SGI material into CGI in previous work.[48] The heating was then turned off for 7.8 minutes, allowing the temperature in the metal to drop to 1300 °C. One of three cooling conditions were subsequently imposed. The highest cooling rate (H) of
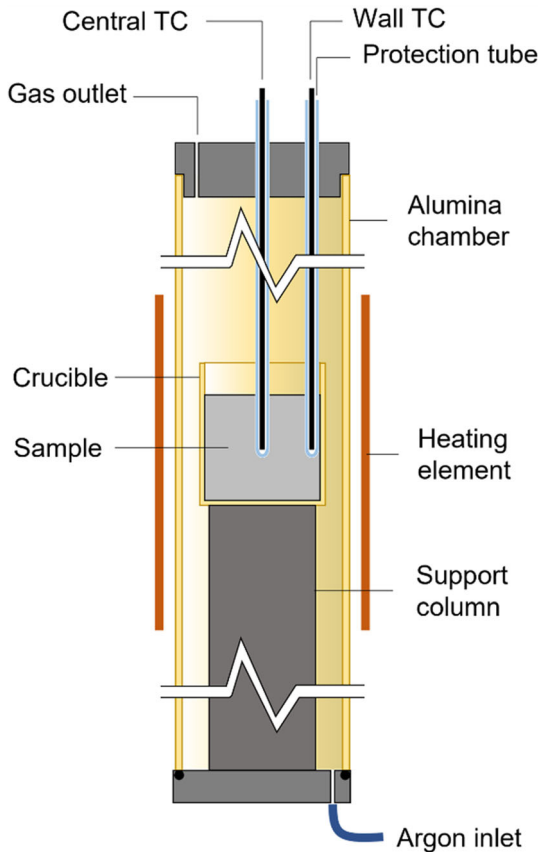
Fig. 1—Schematic illustration of the experimental setup.

0.23 K/s was achieved by leaving the furnace off, allowing the cooling of the metal to proceed without interruption along with the furnace. The medium and low (M and L) cooling rates were achieved by utilization of the control unit to ramp down the temperature at a constant rate from 1300 °C. In line with previous work on LGI,[31] cooling rates of 0.08 and 0.04 were chosen for medium and low cooling rate. The reason for cooling the castings identically until 1300 °C is to reduce the potential impact of prolonged exposure to elevated temperatures on the melt conditions for nucleation and graphite morphology. Table II presents a summary of the furnace programs.

A preliminary set of experiments were performed to record cooling curves for the three cooling conditions. Note that these were mainly used to obtain information necessary for planning of the latter experiments where solidification is interrupted using water quenching.

C. Recording Cooling Curves

The temperature was measured in the positions indicated in Figure 1: one near the center line, and one near the inner crucible wall, both at a height of around half the cylinder. S-type (Pt-Rd, Pt) thermocouples were employed, connected to a commercial temperature

logging unit using extension wires. Thermocouples were protected using Ø5 mm quartz glass tubes sealed in one end using an oxyfuel torch. Experience had shown that the glass tubes tend to deform if left in the intended positions for the full heating cycle. The intended positions of the tubes relative to the top lid were instead marked in advance using O-rings. The thermocouple-tube assemblies were then placed about 300 mm above the intended height. They were finally introduced to the liquid metal 10–20 minutes prior to the end of holding time.

Graphite characterization of preliminary trials verified that the percent nodularity was below 20 pct and contained no lamellar graphite as required for CGI according to ISO 16112:2017(E).

D. Quenching Technique

Water quenching is a proven technique to study solidification of cast irons.[31,32,38,49–57] It is utilizes the fact that rapid cooling forces the residual liquid to form a metastable eutectic manifesting as a fine mix of cementite and austenite, called ledeburite. The former solidified structure is can be distinguished from the latter ledeburite using an appropriate etching technique.

The aim of the water quenching is to study the progress of solidification. Five positions A, B, C, D, E on the cooling curves were chosen according to the following principles:

A: Minimum temperature before recalescence.
B: Maximum temperature during recalescence.
C: Central temperature 1140 °C
D: Mid-point between B and E with respect to time
E: The end of solidification

The positions A–E are indicated on the cooling curves in Figure 2. A count-down timer was employed to keep the quenching schedule. When the timer reached zero, the bottom lid of the furnace was quickly removed, allowing the sample to plunge into a water bath beneath. The graphite pieces and crucible holding the metal are captured in an under-water steel wire basket. A tube connected to a strong water pump is aimed at the bottom of the steel wire basket, causing a strong turbulent flow around the cooling metal.

E. Dendrite Age

As the dendritic austenite evolves over time, its age is of importance. The local age is unknown as it varies between the nucleation point of the grain and its periphery. The age is in this work defined as $t_D = t - t_{ref}$ where t is the concurrent time and t_{ref} is a reference time chosen to be near the time when the first austenite nucleated. This is assumed to occur prior to recalescence, when the second order derivative of the thermocouple placed against the crucible wall begins to raise considerably above the baseline. The reference times are indicated on the cooling curves in Figure 2. The ages for the time of the quench positions A–E for cooling rates H–L are found in Table III.

F. Metallographic Preparation

The solidified metal cylinders were cut using wet abrasive cutting with a disk suitable for cutting hard steels.

Specimens from the preliminary trial where cooling curves had been recorded were cut along the glass tubes which had protected the thermocouples. The measured height of the glass tubes over the bottom of the crucible was 24.5 mm (SD 1.2 mm). The central thermocouple had an average deviation from the center of 3.4 mm. The outer thermocouple was always found resting against the crucible wall.

The quenched specimens were cut horizontally, perpendicular to the center line. Due to the hardness of the quenched materials, the cut tended to end up at an angle. A plane grinding wheel was used to level out the cross sections and adjust the height between 23 and 26 mm above the cylinder base.

The cross sections were ground using Silica paper from grit sizes FEPA P 80 to P 2000 using automated equipment. The ground surfaces were then polished using a 3 μm diamond suspension on a polishing cloth.

To enable distinction between ledeburite and martensite, the quenched cross sections were colored using a novel technique.[58] The coloring is achieved by polishing the specimens using the commercial diamond suspension Struers DiaPro Nap B1 at only 5 N of force for 2 minutes and 20 seconds. The result was controlled using an optical light microscope. In case the coloring was not strong enough, additional polishing was added in steps of 20 seconds.

G. Microscopy

Micrographs were captured using a light optical microscope Olympus GX71F at $10\times$ objective lens magnification across a diameter of the cross section with an overlap of about 40 pct. These were then assembled into a panorama image using the software Image Composite Editor. Each panorama was then divided into 20 equally sized mutually exclusive images. For each cross section, the quantitative microstructure data from the 20 regions was combined into 10 averages of the regions at equal distance from the center as illustrated in Figure 3.

Table II. The Furnace Program Parameters for the Cooling Conditions H, M and L

Cooling Condition	Ramp-Up Time to 1723 K (1450 °C) [min]	Holding Time at 1723 K (1450 °C) [min]	Furnace Off Before Controlled Cooling [min]	Cooling Rate [K/s]
H	90	60	—	0.23[a]
M	90	60	7.8	0.08
L	90	60	7.8	0.04

[a]The highest cooling rate was achieved by simply keeping the furnace off. The given cooling rate is for a secant between 1533 K and 1433 K (1260 °C and 1160 °C).

Table III. Age of Dendritic Austenite at Quench Positions A–E Under Cooling Conditions H–L

Quench position	Age of dendritic austenite at time of quench [s]		
	H	M	L
A	127.3	206	150
B	307.3	518	612
C	601.3	998	1338
D	631.3	1070	1626
E	955.3	1622	2640
Standard deviation	5.5	26.5	62.9

The standard deviation corresponds to variation in the reference time obtained from cooling curves.
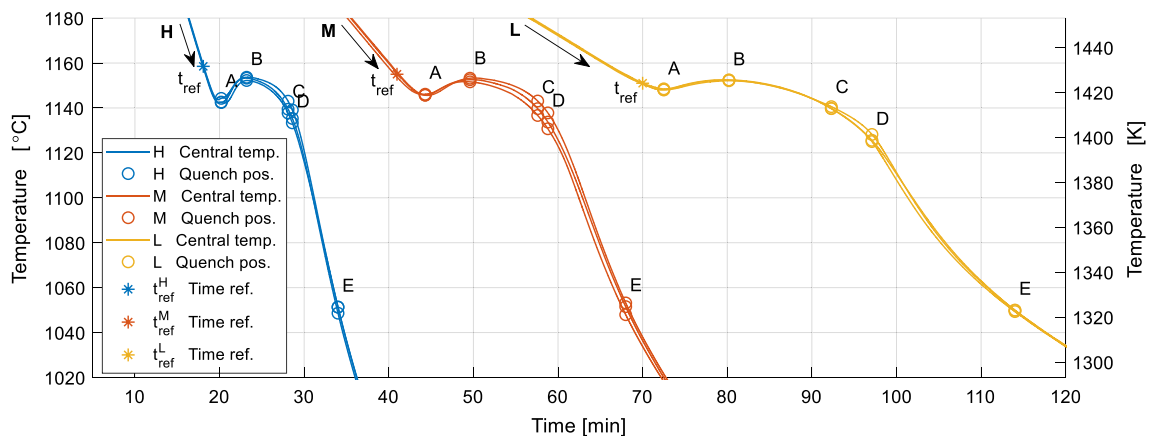

Fig. 2—Cooling curves for the central thermocouple at cooling conditions H, M and L. Solidification was interrupted through quenching at positions A–E.

H. Microstructure Quantification

An example of the microstructure to be quantified is provided in Figure 4, showing the first few millimetres of a sample cooled at medium rate M and quenched at position B. In the micrograph are compacted graphite eutectic cells, graphite nodules with austenite (now martensite) halos, and dendrites. The darker colorful background is ledeburite, which was liquid prior to the quench.

The microstructural features of interest were not possible to segment satisfyingly using automated methods based on color and shape. Micrographs were for this reason first treated by manually segmenting the microstructure using an interactive pen display WACOM DTZ2100/G and the commercial software

Fig. 3—Illustration of how micrographs were sampled from the cross sections.

Adobe Photoshop CC. The micrographs were segmented according to categories defined in Table IV which also includes the corresponding color code and superscripts which are used from here on. An example of a raw and a segmented micrograph is shown in Figures 5(a) and (b) respectively.

Measurements on the treated micrographs are performed with the help of a MATLAB script which recognized the categories based on pixel color. The area fraction of a specific category is calculated as

$$A_A = \frac{N}{N^{tot} - N^X}, \qquad [1]$$

where A_A and N are the area fraction and number of pixels in the specific category and N^{tot} is the total number of pixels in the image and N^X is the number of pixels in the excluded category.

The area fraction A_A is assumed to be equivalent to the volume fraction V_V near the plane of the cross section according to Eq. [2].

$$V_V = A_A. \qquad [2]$$

The script also measures the length of the boundaries between categories. The boundary length L_{pix}, measured in units of pixels, is assumed to be the average of the interior boundary length $L_{interior}$ and the exterior boundary length $L_{exterior}$ according to Eq. [3].

$$L_{pix} = w_L \frac{L_{interior} + L_{exterior}}{2}, \qquad [3]$$

$L_{interior}$ and $L_{exterior}$ were approximated as a weighted sum of vertical, horizontal, and diagonal distances between boundary pixels converted to meters using the pixel length $L_{m/pix}$. The weight w_L in Eq. [3] corresponds to Eq. [4] which counteracts the bias associated with such representation of the boundary.[59]

$$w_L = \frac{\pi}{8(\sqrt{2} - 1)} \approx 0.94806. \qquad [4]$$

The boundary length per unit area L_A in units of $[m^{-1}]$ was calculated as

$$L_A = L_{m/pix}^{-1} \frac{L_{pix}}{N_{total} - N_X}. \qquad [5]$$

where L_{pix} is the length in pixels and $L_{m/pix}$ is the length per pixel in units of meters.
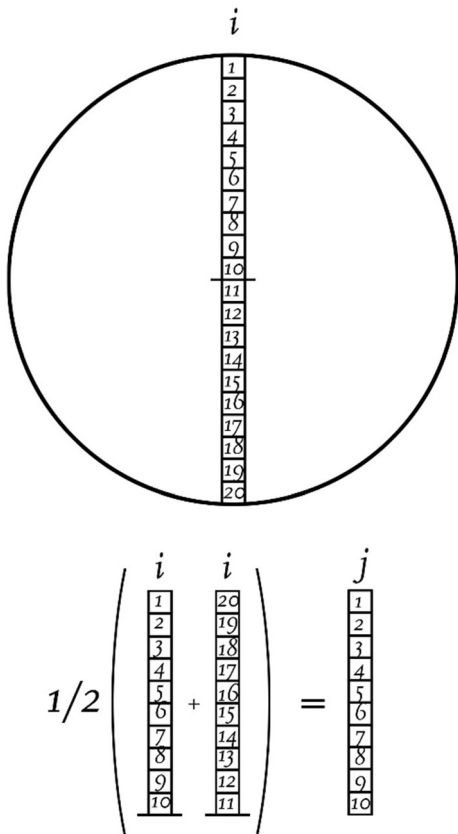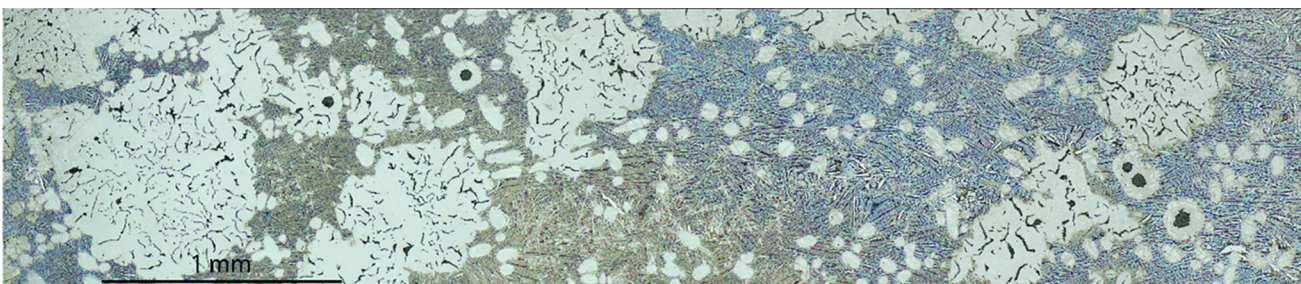

Fig. 4—An example micrograph of the microstructure to be quantified. The crucible wall is to the left.

Table IV. Description of the Categories and Its Respective Color Code and Superscript

Name	Superscript	Category Description	Color Code
Eutectic	E	envelope of graphite-austenite (martensite) eutectic, including engulfed dendritic austenite (martensite)	blue
Dendrites	D	dendritic austenite (martensite) which formed prior to quenching	red
Excluded	X	excluded: large cracks, porosites and edge of sample.	green
Solid	S	solid: the union of E and D	red + blue
Liquid	L	liquid: Everything not S nor X	white
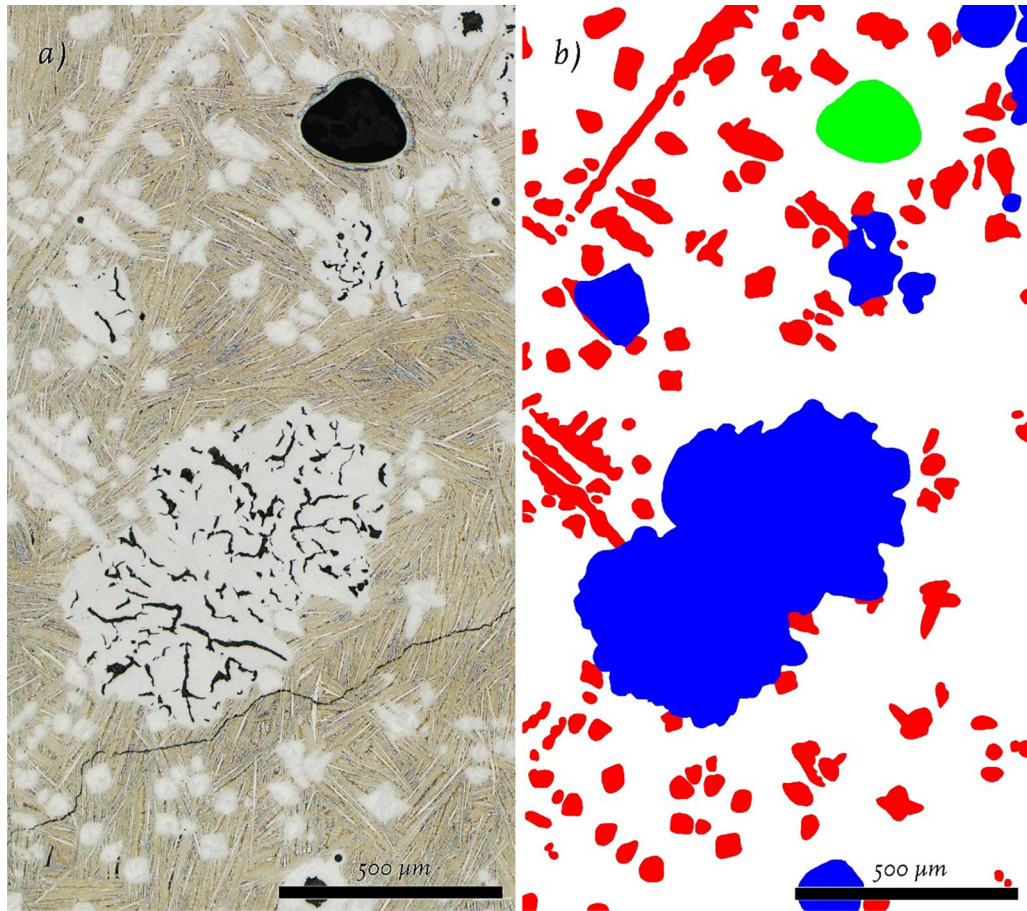
Fig. 5—An example of (*a*) a raw and (*b*) a manually treated micrograph which has been segmented according to categories in Table IV.

The surface area per unit volume S_V is estimated from the boundary length per image area L_A using the stereological relation in Eq. [6].[60]

$$S_V = \frac{4}{\pi} L_A,$$ [6]

V_V and S_V may vary along the height of the cylinder, so translations into volumetric units are only assumed to be valid near the plane of the cross section and cannot be generalized to the full volume of the specimen.

I. Average over the Cross Section

Strictly speaking, the microstructure data was not sampled randomly from the cross-section area, but as a series of adjacent areas along a diameter of randomly chosen orientation. The probability of a given point on the cross section being included in the sample diminishes with distance from the center. Consequently, the mean of the samples across the diameter is not representative of the mean of the cross-section but has a bias towards its center.
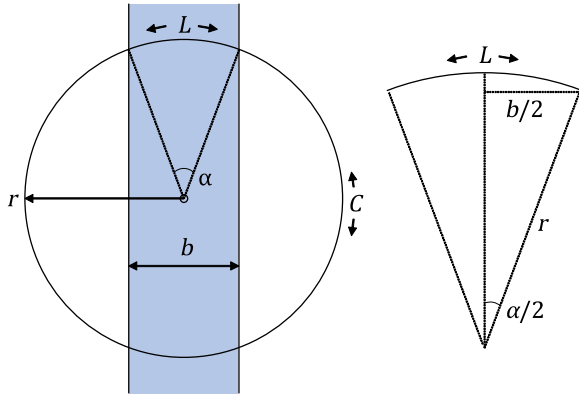
Fig. 6—Schematic illustration of the panoramic picture (blue) crossing the circle on which a given point is located (Color figure online).

In order to compensate for the bias, inverse probability weighting is applied.[61] The mean of the cross section is calculated as a weighted arithmetic mean $\overline{x}_w$ of the n samples

$$\overline{x}_w = \sum_{i=1}^{n} w_i x_i, \qquad [7]$$

where x_i and w_i are the sample values and corresponding normalized weights. The weights are the inverse of probability p_i normalized by the sum of inverse probabilities.

$$w_i = \frac{p_i^{-1}}{\sum_{i=1}^{n} p_i^{-1}}. \qquad [8]$$

The probability p_i of a point at radius r_i being included in the sample region with width L is the fraction of the circumference of a circle with radius r_i being included in the sample region

$$p_i = \frac{2L_i}{C_i}, \qquad [9]$$

where C and L are the circumference and arc length as portrayed in Figure 6.

The circumference and arc length are

$$C_i = \pi 2 r_i, \qquad [10]$$

$$L_i = \alpha_i r_i, \qquad [11]$$

using the arcsine for a triangle with the hypothenuse r_i and half of the sample width b as the opp where α_i is the arc angle in radians. The arc angle is found, as illustrated in Figure 6 using the arcsine for a triangle with the hypothenuse r_i and half of the sample width b as the opposite side length.

$$\alpha_i/2 = sin^{-1}\left(\frac{b/2}{r_i}\right). \qquad [12]$$

Inserting Eq. [12] in [11] and then inserting Eqs. [10] and [11] in [9] and gives the probability

$$p_i = \frac{2}{\pi} sin^{-1}\left(\frac{b/2}{r_i}\right). \qquad [13]$$

To find the weights for the 20 panorama segments the radius r_i in Eq. [13] is taken as the radial distance from the centre of the cross section to the centre of a given segment, after which the resulting probabilities are used in Eq. [8]. Weighted arithmetic means are then calculated using Eq. [7].

III. RESULTS AND DISCUSSION

Specimens quenched at positions E contained no apparent ledeburite which could be interpreted as having been liquid at the time of the quenching. The microstructure was for this reason not characterized in these specimens.

A. Quench Dendrites and Measurement Bias

Before the results are presented, a source of potential measurement bias is discussed. It is known from previous research that a second set of fine austenite dendrites tends to grow when a cast iron is– quenched during solidification.[62] These are from here on referred to as quench dendrites. Under certain conditions in this study, it was difficult to differentiate between the prior dendrites which had grown during furnace cooling and the latter quench dendrites. The risk of conflation increases the more similar the two are in scale. Prior dendrites are finer at earlier stages of solidification and at high cooling rates. Moreover, the quench dendrites were found to be coarser towards the center of the casting, presumably due to the slower cooling. Consequently, the risk of conflation is the highest at the center of cross section for the highest cooling rate H and the first quench position A. Even in this case, the dendrites formed during the quenching were easily distinguished from the prior dendrites near the surface of the casting but became increasingly similar towards the center. The issue was present to a lighter degree also in B for the same cooling condition and in A for the cooling condition M, but for the remaining specimens this was not an issue.

B. Variation Along the Radius

Before the measurements are summarized into mean values, the variation of the measurements along the radius of the cross sections is examined.

Figure 7(a) shows that almost no eutectic is present at the first quench position A for the highest cooling rate H. At the next quench position B, the volume of eutectic envelopes V_V^E has grown, particularly close to the surface of the specimen. By quench positions C and D, the eutectic envelopes cover the dominant area of the cross sections and, again, more so towards the surface. At lower cooling rates M and L in Figures 7(b) and (c), the eutectic tends to have a more uniform distribution over the cross section. This seems reasonable considering the temperature difference between surface and centre decreases as the cooling rate is lowered.
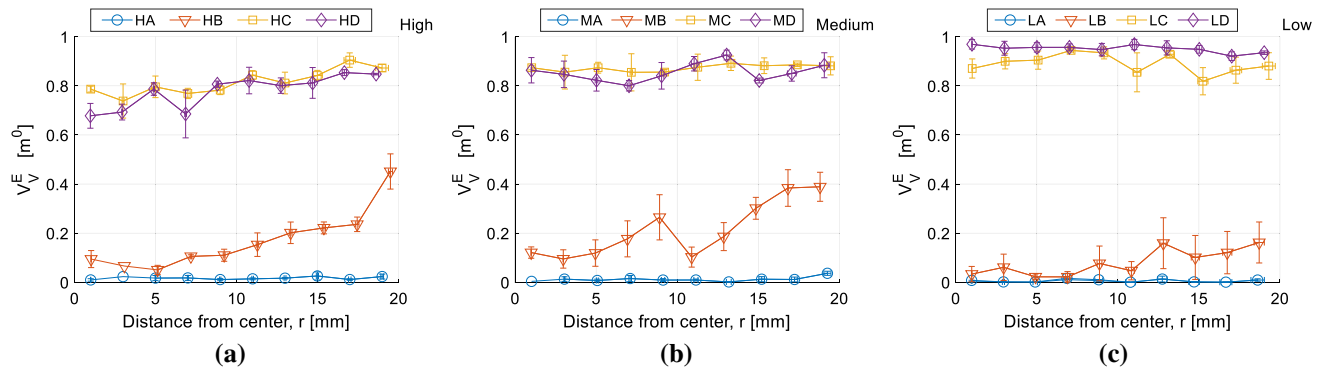
Fig. 7—Volume fraction of eutectic versus distance from the center of cross sections. Cooling conditions (*a*) H, (*b*) M, (*c*) L. Error bars indicate the standard error of the mean for the repetitions. In cases where error bars are absent, the mean is based on less than three repetitions due to local absence of eutectic envelopes.
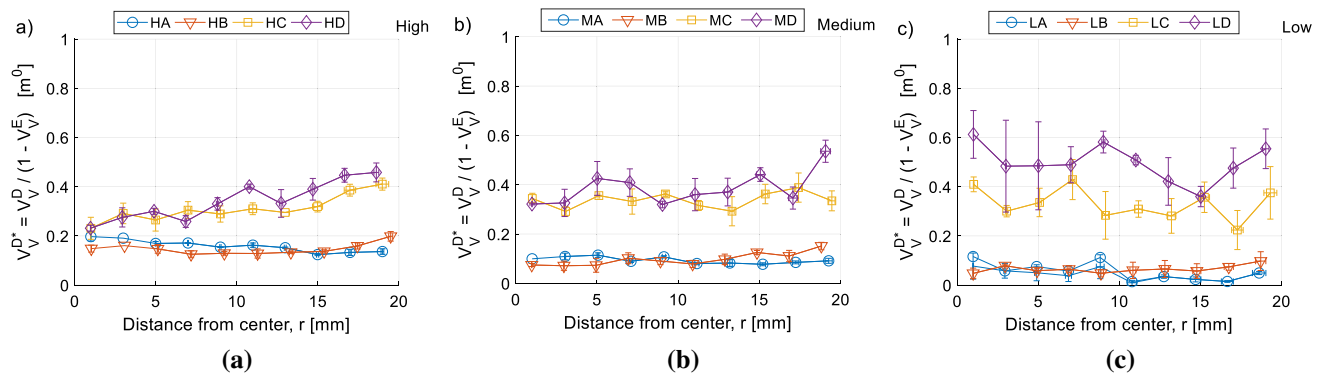

Fig. 8—Volume fraction dendrites in extra-eutectic regions versus distance from the center of cross sections. Cooling conditions (*a*) H, (*b*) M, (*c*) L. Error bars indicate the standard error of the mean for the repetitions. In cases where error bars are absent, the mean is based on less than three repetitions due to local absence of dendritic austenite.

The total volume fraction of dendritic austenite decreases as these are engulfed in the eutectic envelopes, so it is more meaningful to study the evolution of the volume fraction of dendritic austenite in the extra-eutectic regions V_V^{D*}, obtained by normalizing the volume fraction of dendrites by the extra-eutectic volume fraction $V_V^{D*} = V_V^D / (1 - V_V^E)$.

Figure 8(a) shows that quench position A for cooling condition H already contains a dendritic austenite network distributed over the cross section, though slightly higher towards the center of the cross section. The latter may relate to increased likelihood of inclusion of quench dendrites, as discussed in the previous subsection. This would also explain why, contrary to expectation, V_V^{D*} appears to have decreased slightly in the central region by quench position B. At the later quench positions C and D, the V_V^{D*} has increased considerably and like V_V^E, V_V^{D*} tends to be higher towards the surface of the specimen. According to Figures 8(b) and (c), V_V^{D*} is generally lower for quench positions A and B and higher for C and D at

lower cooling rates M and L. This is treated further in the next Sect. III–C by looking at the average V_V^{D*} over the cross sections.

Figures 9(a) through (c) shows that the modulus of dendritic austenite M^D is relatively uniform over the cross section for all cooling conditions at the first two quench positions A and B. For the highest cooling rate H the modulus M^D is also relatively uniform at quench positions C and D, but for the slower cooled M and L the modulus displays more scatter. This scatter is likely related to the smaller sample size of dendritic austenite as a result of being engulfed in eutectic as can be observed in Figure 7.

Others researchers have observed considerable differences in the secondary arm spacing of dendrites along the radius of a cylindrical specimen in Sn–Pb alloys, which they found to correlate with variations in the tip growth rate.[63] Moreover, if the dendritic austenite nucleated at the crucible wall and grew towards the centre, the dendritic structure near the wall would have had more time to coarsen than in the centre.
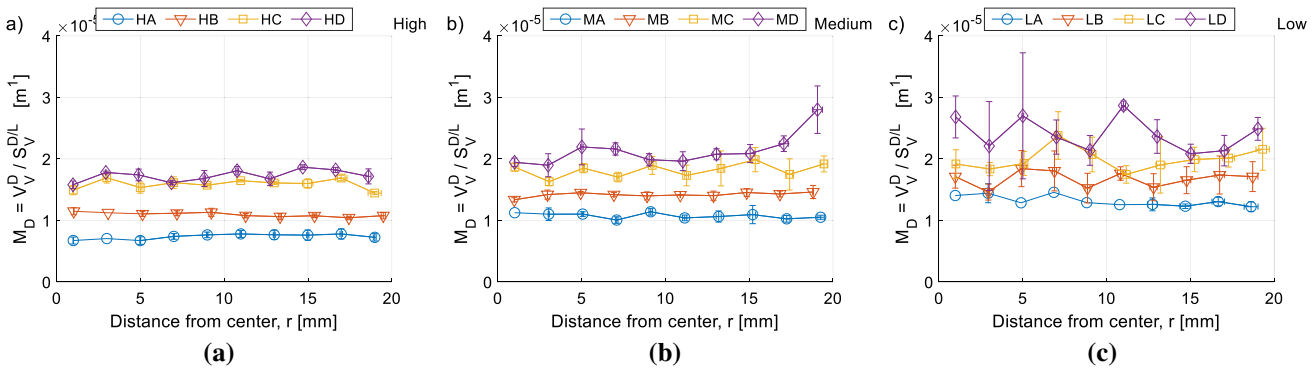
Fig. 9—Modulus of dendritic austenite versus distance from the center of cross sections. Cooling conditions (*a*) H, (*b*) M, (*c*) L. Error bars indicate the standard error of the mean for the repetitions. In cases where error bars are absent, the mean is based on less than three repetitions due to local absence of dendritic structure.

The observation that M^D is almost uniform across the sections indicates that the combined influence of variations in tip growth rate and variations in coarsening time was in the present case small relative to the influence of the total coarsening time. This means that M^D over a cross section is fairly represented by an average, which simplifies analysis of its evolution over time.

C. Volume Fraction of Dendritic Austenite

Figure 10 shows the extra-eutectic volume fraction of dendrites for cross sections, ranging from 0.02 to 0.59, showing dependence both on cooling rate (H, M, L) and appears to rise through solidification. An equilibrium calculation for the chemical composition in Table I using Thermo-Calc 2022a with the TCFE7 databank suggests that the alloy is slightly hypereutectic, with 0.2 vol. pct graphite at the onset of eutectic. This suggests that all measured dendrites are in excess of primary austenite expected at equilibrium.

Previous work on LGI has shown volume fraction dendrites of about 0.2 in excess of equilibrium, measured based on microsegregation patterns.[37] Given that the volume fraction in this work rises while engulfed in eutectic, comparison to measurements based on colour-etching of as-cast iron is not straight forward. However, the increase of the volume fraction of extra-eutectic dendrites V_V^{D*} through the solidification interval observed in Figure 10, implies that the engulfed dendritic structure is not uniform in the final material. Rather, the volume fraction of dendrites engulfed in eutectic cells is expected to be lower than average in their centre and rise along their radii to higher than average in last-to-freeze regions. If the dendrites observed using colour etching correspond to its frozen-in state as it was engulfed by eutectic, it is expected to represent the average across the region. The increasing trend in V_V^{D*} observed in Figure 10 is thus roughly in line with the average excess of 0.2 observed in earlier work.[37]
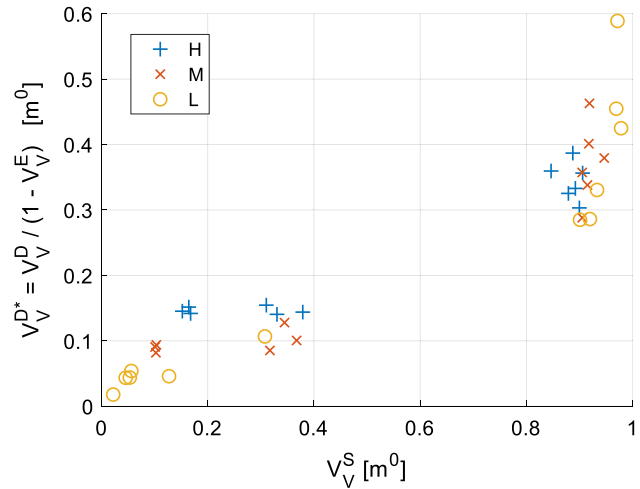

Fig. 10—The measured volume fraction of dendritic austenite in extra-eutectic regions versus the volume fraction of solid. Each data point represents the average over a cross section.

Moreover, Figure 10 shows that, for a given V_V^S, extra-eutectic regions tend to include a higher volume fraction of dendritic austenite V_V^{D*} at higher cooling rates. This is contrary to earlier findings of a similar study of a hypoeutectic LGI, where the measured volume fraction of dendritic austenite is more stable over a similar range of cooling rates.[32] A reasonable explanation for this discrepancy is that the dependency on cooling rate only occur when the dendritic austenite grows in competition with the eutectic. It has for example been reported for a high-purity near-eutectic Fe–C alloy that dendritic austenite is absent below a critical imposed growth velocity.[44] Less dependency on cooling rate can thereby be expected for hypoeutectic compositions, where the dendritic austenite grows considerably in advance of the eutectic. The different growth kinetics of compacted and lamellar graphite may also contribute, as a slower growth of eutectic would leave dendritic growth of austenite more competitive.
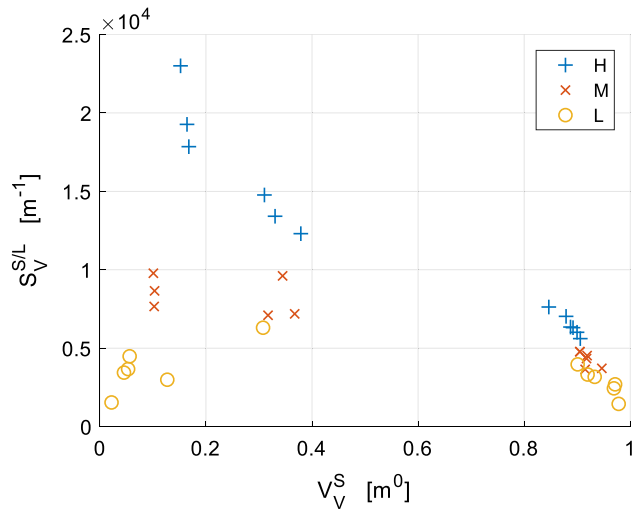
Fig. 11—Surface area of the solid–liquid interface versus volume fraction solid. Each marker represents the mean of a cross section.
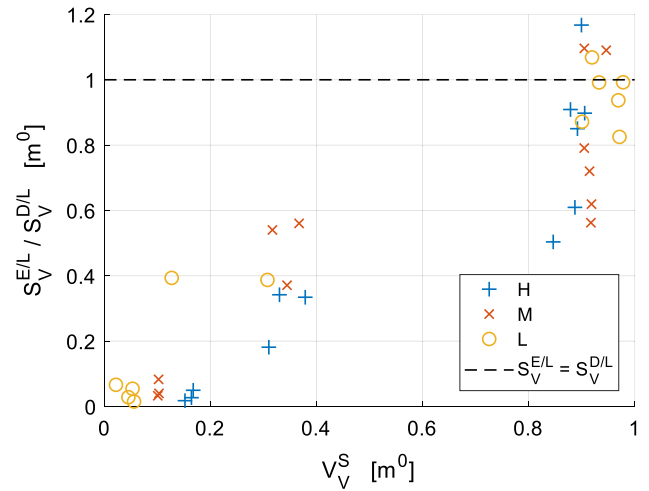

Fig. 12—A comparison of interfacial surface areas against the liquid using the ratio of the surface area of eutectic envelopes and dendritic austenite. Below the dashed line, the surface area of the dendritic austenite is larger than the surface area of eutectic envelopes.

D. Surface Area of the Solid–Liquid Interface

Figure 11 shows that the surface area of the solid–liquid interface $S_V^{S/L}$ is initially considerably larger at higher cooling rates. This can be understood as a combination of larger V_V^{D*} as shown in Figure 8 and a finer dendritic structure which carries more surface per unit volume as will be shown in Sect. III–E.

Figure 11 also shows that differences in $S_V^{S/L}$ between the three cooling rates tend to decrease as solidification proceeds. Yet, differences seem to persist even at the latest observed stages of solidification. The rapid decline of $S_V^{S/L}$ for the highest cooling rate H is likely a result of phase coarsening, engulfment of dendritic structure by the eutectic and impingement of eutectic cells. At medium cooling rate M, the decrease in $S_V^{S/L}$ was less prominent. Data is scarce for intermediate solid fractions for the slowest cooling rate L, but the data indicates that there may be a local maximum at an intermediate solid fraction. Growth of $S_V^{S/L}$ is associated with growth of new dendritic structure as indicated by Figure 10, while decrease of $S_V^{S/L}$ is associated with dendrite coarsening and engulfment of dendrites by the eutectic, which, as will be shown hereafter, has less surface area against the liquid.

Figure 12 shows that the surface area of the eutectic envelopes against the liquid initially constitute a small fraction of the total solid–liquid interface. It is only beyond $V_V^S \approx 0.9$, that the eutectic has larger contact area with liquid than dendritic austenite. The increasing proportion is likely a combination of the growth of the eutectic–liquid interface, the engulfment of dendritic austenite and the coarsening of the residual dendritic austenite structure.

In practice, inoculation is typically applied to promote smaller and more numerous eutectic cells. The trend presented in Figure 12 is thus expected to shift upwards under conventional conditions, such that the

eutectic has the larger surface area against the liquid than the dendritic austenite during the later stage of solidification.

E. Coarsening of the Modulus of Dendritic Austenite

The coarseness of the dendritic austenite is in this work characterized by its modulus M^D, which has been shown to evolve according to a fairly stable relation to time under isothermal conditions.[5] Figure 13 shows the mean M^D over the cross sections against the cube root of the dendrite age $t_C^{1/3}$. The figure also includes extrapolations from the earliest measured modulus using the proportionality to $t_C^{1/3}$, reported for isothermal coarsening experiments on LGI.[5] The slope of dotted lines in Figure 13 is the rate coefficient $k_M = 9.63\text{E}{-}7$ ms$^{-1/3}$ which is taken from the cited work (with a correction for the neglected stereological factor $4/\pi$).[5]

It is clear from Figure 13 that the extrapolation underestimates the increase in M^D over the solidification interval, particularly for higher cooling rates. This agrees with research findings for other alloy systems, where the deviation has been attributed to growth by thickening of existing dendrites.[23,64]

Compared to isothermal conditions, the present case introduces at least two important factors: (1) the temperature decreases and (2) the volume fraction of dendrites increases.

The temperature is in the present work always lower than 1175 °C at which the coarsening rate k_M was measured under isothermal conditions.[5] As dendrite arm coarsening in alloys depends on solute diffusion in the melt,[26–28] which rate is well known to increase with temperature, the rate k_M is expected to fall along with the diffusivity when the temperature drops. For this reason, the present temperature conditions are expected to result in a slower coarsening process compared to the reported isothermal case.
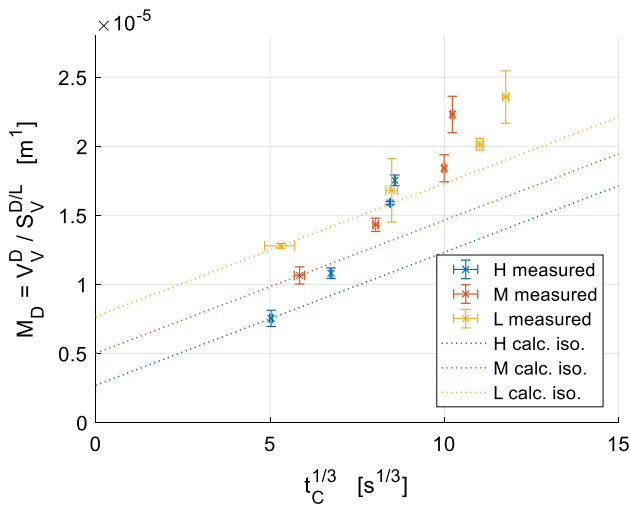
Fig. 13—Modulus of the dendritic structure as a function of the cube root of the dendrite age. Vertical bars are the standard error of the modulus for three repetitions. Horizontal bars are the standard error of the time for start of solidification, obtained from cooling curves. Dotted lines are extrapolations from the earliest measured modulus based on a reported evolution of the modulus under isothermal conditions [5]

As was shown in Figure 8, the volume fraction of austenite dendrites in extra-eutectic regions $V_V^{D*} = V_V^D/(1 - V_V^E)$ increases through the solidification interval. In other alloy systems, the isothermal coarsening rate has been shown to increase with solid fraction, which has been attributed to shortened diffusion distances between high and low curvature interfaces through the melt.[26] While the influence of temperature and solid fraction on k_M is not known for cast irons, the used k_M was measured at a V_V^S of 0.38 with a standard deviation of 0.05.[5] As the volume fraction of dendritic austenite in extra-eutectic regions $V_V^{D*} < 0.38$ through most of the interval A–D, k_M is expected to be generally lower in the present case. Only a slight increase of k_M may be expected over the brief interval C–D for slow and medium cooling, where $V_V^{D*} > 0.38$.

As the present conditions of both temperature and V_V^{D*} are expected to lower the coarsening rate k_M while as the M^D increased at a higher rate, it appears the impact of these factors on the modulus is relatively small.

F. Growth of Dendritic Austenite During Eutectic Solidification

Besides influencing the kinetics of the coarsening process, the increase in V_V^{D*} also implies that the dendritic austenite structure has grown, which can be expected to alter the balance between volume and surface area of the dendritic structure and thereby its modulus. It follows from the definition $M^D = V_V^D/S_V^{D/L}$ that the modulus increases in proportion to an independent increase of V_V^D. However, growth of the structure also contributes to a change in $S_V^{D/L}$, as discussed by other researchers.[23,64]
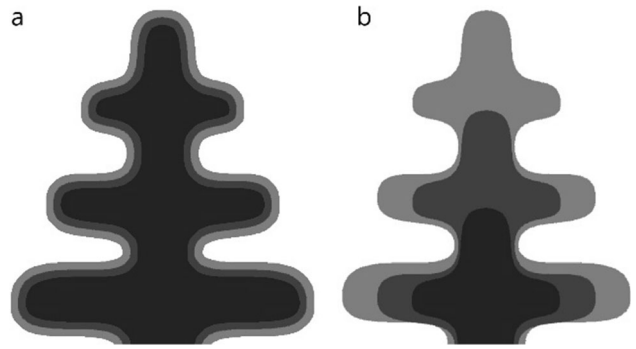

Fig. 14—Illustration of growth modes (a) thickening and (b) tip growth. The darker shades represent earlier states of the dendritic structure.

In general, growth of the dendritic structure seems to occur by some combination of (1) tip growth, generating new fine dendritic structure with large surface area and (2) growth normal to the existing dendrite surface, which is hereby referred to as thickening. Figure 14 illustrates how these modes change the relation between volume and surface area and therefore the M^D in different ways. The thickening of the structure in Figure 14(a) is expected to increase the volume more than the surface area, resulting in an increase of M^D. This is easily shown to be true for simple geometries such as cylinders and spheres, where M^D increases in proportion to the radius. On the other hand, tip growth illustrated in Figure 14(b) is expected to result in generation of new dendritic structure which has a small M^D relative to the earlier structure which has undergone coarsening. In other words, tip growth dilutes the average modulus, causing a decrease towards the initial modulus. While both mechanisms may have been present, only thickening of existing dendrite arms has potential to explain the elevated coarsening rate of M^D relative to the isothermal case.

The dendritic austenite structure displayed poor coherency in quench positions A and B, particularly at lower cooling rates. This can to an extent be observed in Figures 15(a) through (f). Coherency was particularly poor for cooling conditions M and L, where large fields without dendrites were observed. This suggests that there was plenty of room for additional dendrite tip growth to occur. It has been reported for LGI that the dendritic austenite grows by means of tip growth until a volume fraction of $V_{V,crit}^{D*} = 0.32$ after which the dendrite arms grow by thickening.[34] As V_V^{D*} is for the most part lower than 0.32, this suggests that the observed increase in V_V^{D*} is mostly a consequence of tip growth.

It is not easily confirmed that the structure has grown by tip growth from B to C and D. Figures 15(g) through (l) provide some examples of dendritic structure which appears to be finer than expected considering the evolution of the average modulus previously shown in Figure 13. A closer examination of a pair of dendritic structures with what appears to be regularly spaced secondary arms is provided in Figures 16(a) and (b), which were observed under cooling condition L for
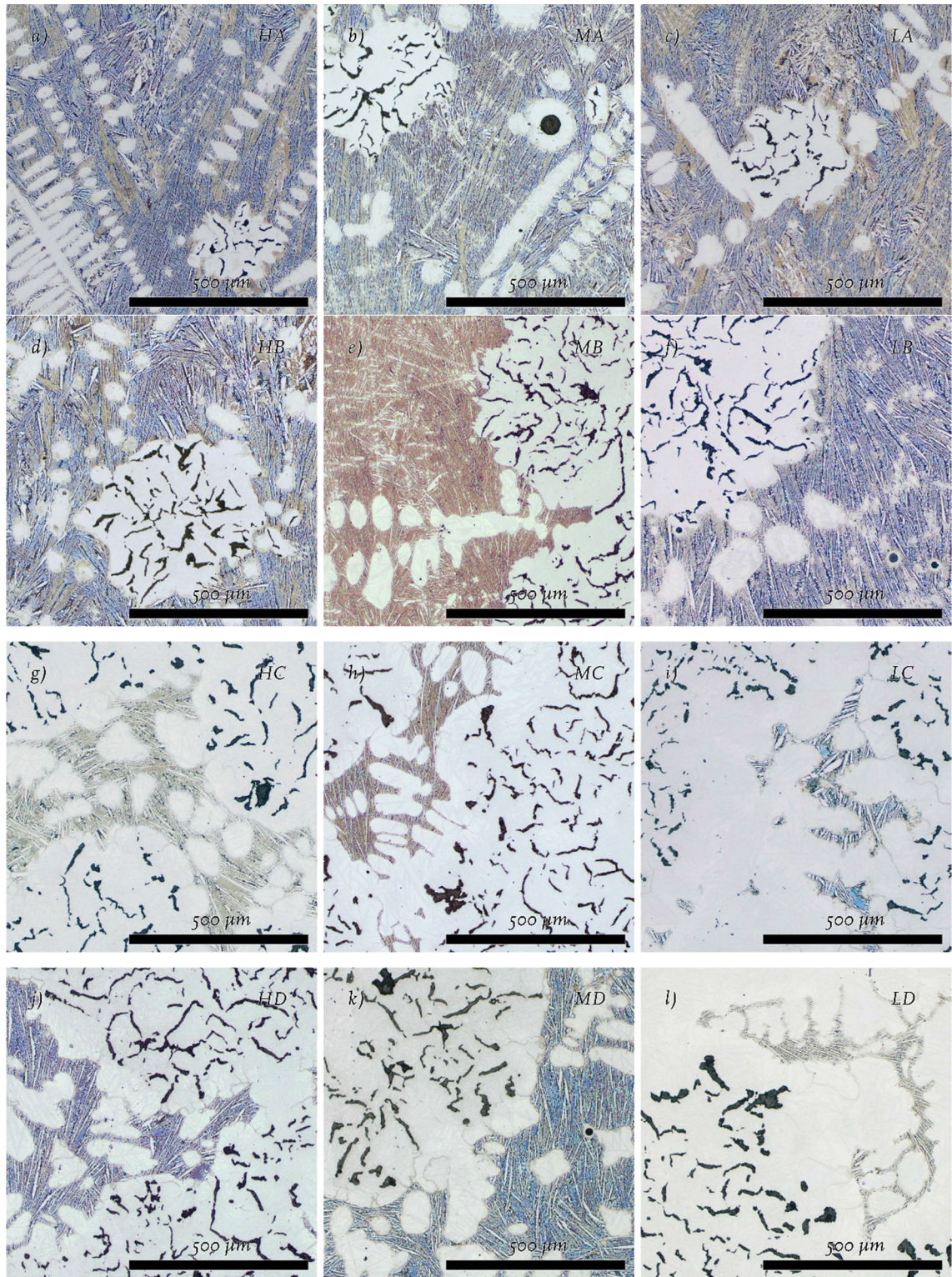
Fig. 15—Examples of the quenched microstructure in (*a*) HA, (*b*) HB, (*c*) HC, (*d*) HD, (*e*) MA, (*f*) MB, (*g*) MC, (*h*) MD, (*i*) LA, (*j*) LB, (*k*) LC, (*l*) LD.

quench positions B and C respectively. The average spacing between secondary arms (SDAS) was measured in the two micrographs, giving values of 62 and 52 μm respectively. A comparison to the reported evolution of SDAS under isothermal conditions[5] suggests 62 μm

corresponds to an age in the neighborhood of 8 $s^{1/3}$ (512 seconds) which is in fair agreement with the dendrite age of position B. However, the smaller spacing of 52 μm in C appears to be severely of out of place considering the longer dendrite age of 11 $s^{1/3}$
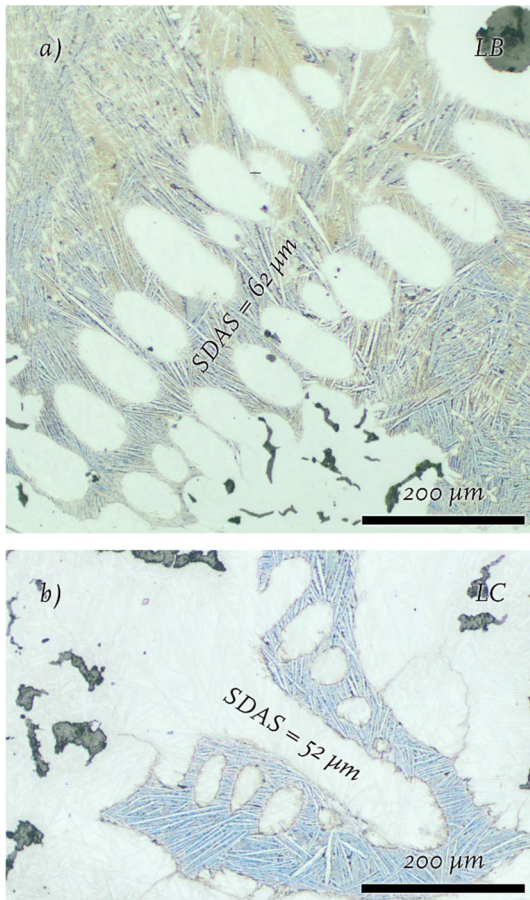
Fig. 16—Examples of well defined secondary arms from quench positions (*a*) B and (*b*) C, both under the lowest cooling rate L. The smaller average spacing between secondary arms in b suggests that dendrite tip growth occurred after quench position B.

(1331 seconds). Assuming that the initial SDAS after tip growth is constant, the SDAS of 52 μm suggests the structure observed for C in b is younger than the time elapsed between B and C.

This evidence of tip growth is of course anecdotal and there is a risk that the dendrite arms measured in Figure 16(b) are ternary rather than secondary. Yet, it appears reasonable that some portion of the observed increase in V_V^{D*} between B and C under cooling condition L is the result of tip growth.

The data presented in Figure 13 shows that the modulus after the first observation appears to consistently increase at a higher rate than expected under pure isothermal coarsening. As both the fall in temperature and the increase in solid fraction are expected to reduce k_M and tip growth is expected to decrease the average modulus, this suggests that other mechanisms which contribute to a rise in the modulus are dominant. As models accounting for growth by thickening has shown good agreement with experimental data for other alloys, it appears reasonable that this is an important contributor to the observed increase in M^D also in this case.[23,64]

Of the factors considered in this paper, arm thickening appears to be the only factor contributing to a rise in the modulus besides isothermal coarsening. Since the measured increase in M^D over time always exceeded the increase expected under isothermal conditions, arm thickening appears to play an important role in all cases, but less so at slower cooling.

G. Reliability

As discussed in Sect. III–A, there is risk of conflation of dendrites which grew before and during the quench. Again, the risk of conflation is highest for the central region of the earliest quenched sample cooled at the highest rate (HA), where the scale of the two are most similar. The error in volume fraction ΔV_V^{D*}, can be estimated from Figure 8 by comparing center and periphery of HA (+ 0.04) as well as comparing the center of HA to the center of HB (+ 0.05). Obviously, by nature of the later estimate, it accounts for the apparent cooling rate dependence of V_V^{D*} in Figures 8 and 10 for the lowest solid fractions. However, given that this cooling rate dependence is persistent through quench positions C and D and cooling rate L, where the error should be negligible, the conclusion that V_V^{D*} is favored by cooling rate appears to hold. ΔV_V^{D*} cannot account for the observed rise in V_V^{D*} towards the late part of solidification, as it is rather expected to cause exaggeration of V_V^{D*} during early solidification. Conflation of prior and quench dendrites is expected to have a minor effect on the M_D, as the highest risk of conflation is highest when M_D of the two is the most similar, meaning it would cause little bias.

Another potential source of error is that the incoherency of equiaxed dendrites noted for QLA, QLB and to a smaller degree in QMA and QMB, allowing them to potentially float in and out of the observed section. This may have affected the measured V_V^{D*}. However, the observed dependence of V_V^{D*} on cooling rate was not limited to the equiaxed zone but was prominent all the way to the crucible wall, where columnar dendrites are found attached to the wall. This gives the impression that while V_V^{D*} may be unreliable locally in the centers of QLA and QLB, this does not account for the observed sensitivity of V_V^{D*} to cooling rate. Movement of equiaxed dendrites is not expected to affect M_D notably, as dendrites floating in or out of plane are likely of similar age and thereby have similar M_D.

IV. REMARKS

It has been observed for the present near-eutectic CGI that higher cooling rate tends to promote a more coherent structure of dendritic austenite which constitutes a higher volume fraction. Moreover, the structure continued to grow through the solidification interval in parallel with the eutectic. The dendritic structure also becomes coarser over time, in terms of having less surface area per volume of dendrites. Given that the

structure is gradually engulfed in the eutectic over the solidification interval, this suggests that the modulus and volume fraction of the dendritic structure is not uniform in the as-cast material, but varies from the earliest parts of the structure engulfed by the eutectic, at the centre of eutectic cells, towards the parts of the structure last engulfed by the eutectic. This seems highly relevant to recent research indicating that the dendritic structure plays an important role in the tensile strength of the material.[18–20]

In order to predict the evolution of the dendritic austenite structure through the solidification of near-eutectic CGI, the main difficulties appear to be to better understand the relation between cooling rate and the amount of dendritic austenite, how much new dendritic structure grows in parallel with eutectic growth, and to what degree this structure grows by means other than thickening, such as tip growth.

V. CONCLUSIONS

The evolution of the dendritic structure in a near-eutectic compacted graphite iron was studied through the solidification interval at three cooling rates using water quenching.

- The total surface area against the liquid was generally larger at higher cooling rates but differences diminished towards the end of solidification.
- The interfacial surface area against the liquid was larger for the dendritic structure than for the eutectic through most of the solidification interval. This indicates that the dendritic structure is an important contributor to feeding issues even for near-eutectic compositions.
- Higher cooling rate promoted a more coherent dendritic austenite structure which generally constituted a higher volume fraction and surface area through the solidification interval.
- Dendritic austenite in extra-eutectic regions continued to change in parallel with growth of eutectic, both in terms of a considerable rise in volume fraction and coarsening as characterized by more volume per surface area of dendrites. This implies that the amount and shape of dendrites engulfed in eutectic varies from centres of eutectic cells towards last-to-freeze zones, contributing to non-uniform dendrite structure in the as-cast material, particularly for near-eutectic or hypereutectic irons.
- The ratio of volume over surface area (modulus) of the dendritic austenite structure increased at a higher rate than previous reports for isothermal conditions. Comparison to studies of coarsening in other alloys suggests that this may be related to the observed rise of the volume fraction by thickening of the structure. On the other hand, evidence of continued tip growth in parallel with eutectic growth was also observed.

CONFLICT OF INTEREST

On behalf of all authors, the corresponding author states that there is no conflict of interest.

REFERENCES

1. M. Basaran: *Metall Trans. A*, 1981, vol. 12(7), pp. 1235–43. https://doi.org/10.1007/BF02642337.
2. J.M. Motz: *Pract Metallography*, 1988, vol. 25(6), pp. 285–93. https://doi.org/10.1515/pm-1988-250605.
3. R. Boeri and F. Weinberg: *AFS Trans.*, 1989, vol. 89, pp. 179–84.
4. R. Boeri and F. Weinberg: *Cast Met.*, 1993, vol. 6(3), pp. 153–58. https://doi.org/10.1080/09534962.1993.11819142.
5. J.C. Hernando, E. Ghassemali, and A. Diószegi: *Mater. Charact.*, 2017, vol. 131, pp. 492–99. https://doi.org/10.1016/j.matchar.2017.07.030.

6. P.C. Carman: *Trans. Inst. Chem. Eng.*, 1937, vol. 15, pp. 150–66. https://doi.org/10.1016/S0263-8762(97)80003-2.
7. P.C. Carman: *J. Agric. Sci.*, 1939, vol. 29(2), pp. 262–73. https://doi.org/10.1017/S0021859600051789.
8. Ø. Nielsen, S.L. Arnberg, A. Mo, and H. Thevik: *Metall. Mater. Trans. A*, 1999, vol. 30(9), pp. 2455–62. https://doi.org/10.1007/s11661-999-0254-y.
9. A. Duncan, Q. Han, and S. Viswanathan: *Metall. Mater. Trans. B*, 1999, vol. 30(4), pp. 745–50. https://doi.org/10.1007/s11663-999-0036-3.
10. D. Poirier and S. Ganesan: *Mater. Sci. and Eng. A*, 1992, vol. 157(1), pp. 113–23. https://doi.org/10.1016/0921-5093(92)90105-A.
11. J. Madison, J.E. Spowart, D.J. Rowenhorst, L.K. Aagesen, K. Thornton, and T.M. Pollock: *Metall. Mater. Trans. A*, 2012, vol. 43(1), pp. 369–80. https://doi.org/10.1007/s11661-011-0823-8.
12. C. Wang, S. Ahuja, C. Beckermann, and H. De Groh: *Metall Mater. Trans. B*, 1995, vol. 26(1), pp. 111–19. https://doi.org/10.1007/BF02648984.
13. J.C. Heinrich and D.R. Poirier: *Comptes Rendus Mécanique*, 2004, vol. 332(5), pp. 429–45. https://doi.org/10.1016/j.crme.2004.02.001.
14. Q. Wang: *Metall. Mater. Trans. A*, 2003, vol. 34(12), pp. 2887–99. https://doi.org/10.1007/s11661-003-0189-7.
15. P.R. Goulart, J.E. Spinelli, W.R. Osório, and A. Garcia: *Mater. Sci. Eng. A*, 2006, vol. 421(1), pp. 245–53. https://doi.org/10.1016/j.msea.2006.01.050.
16. J. Olofsson, I.L. Svensson, P. Lava, and D. Debruyne: *Mater. Des.*, 2014, vol. 56, pp. 755–62. https://doi.org/10.1016/j.matdes.2013.12.036.
17. K.W. Seah, J. Hemanth, and S. Sharma: *J. Mater. Sci.*, 1998, vol. 33(1), pp. 23–28. https://doi.org/10.1023/A:1004321007806.
18. V. Fourlakidis and A. Diószegi: *Mater. Sci. and Eng. A*, 2014, vol. 618, pp. 161–67. https://doi.org/10.1016/j.msea.2014.08.061.
19. V. Fourlakidis, L.V. Diaconu, and A. Diószegi: *Mater. Sci. Forum*, 2018, vol. 925, pp. 272–79. https://doi.org/10.4028/www.scientific.net/MSF.925.272.
20. J.C. Hernando, J. Elfsberg, E. Ghassemali, A.K. Dahle, and A. Diószegi: *Scripta Mater.*, 2019, vol. 168, pp. 33–37. https://doi.org/10.1016/j.scriptamat.2019.04.010.
21. Y. Wu, T. Piccone, Y. Shiohara, and M. Flemings: *Metall. Mater. Trans. A*, 1987, vol. 18(5), pp. 915–24. https://doi.org/10.1007/BF02646933.
22. R. Trivedi and W. Kurz: *Int. Mater. Rev.*, 1994, vol. 39(2), pp. 49–74. https://doi.org/10.1179/imr.1994.39.2.49.
23. N.J. Whisler and T.Z. Kattamis: *J. Cryst. Growth*, 1972, vol. 15(1), pp. 20–24. https://doi.org/10.1016/0022-0248(72)90315-6.
24. P.W. Voorhees: *J. Stat. Phys.*, 1985, vol. 38, pp. 231–52. https://doi.org/10.1007/BF01017860.
25. S. Hardy and P. Voorhees: *Metall. Mater. Trans. A*, 1988, vol. 19(11), pp. 2713–721. https://doi.org/10.1007/BF02645806.
26. S.P. Marsh and M.E. Glicksman: *Metall. Mater. Trans. A*, 1996, vol. 27A, pp. 557–67. https://doi.org/10.1007/BF02648946.
27. R. Mendoza, J. Alkemper, and P. Voorhees: *Metall. Mater. Trans. A*, 2003, vol. 34A(3), pp. 481–90.
28. D. Kammer and P. Voorhees: *Acta Mater.*, 2006, vol. 54(6), pp. 1549–558. https://doi.org/10.1016/j.actamat.2005.11.031.
29. M. Gündüz and E. Çadırlı: *Mater. Sci. and Eng. A*, 2002, vol. 327(2), pp. 167–85. https://doi.org/10.1016/S0921-5093(01)01649-5.
30. K. Young and D. Kerkwood: *Metall. Trans. A*, 1975, vol. 6(1), pp. 197–205. https://doi.org/10.1007/BF02673688.
31. R. Lora and A. Diószegi: *Metall. Mater. Trans. A*, 2012, vol. 43(13), pp. 5165–72. https://doi.org/10.1007/s11661-012-1244-z.
32. A. Diószegi, R. Lora, and V. Fourlakidis: *Mater. Sci. Forum*, 2014, vol. 790–791, pp. 205–10. https://doi.org/10.4028/www.scientific.net/MSF.790-791.205.
33. F. Mampaey, Z.A. Xu: *62nd World Foundry Congr.*, 1996, pp. 1–11.
34. F. Mampaey: *AFS Trans.*, 1998, vol. 106, pp. 469–76.
35. G.L. Rivera, R.E. Boeri, and J.A. Sikora: *Cast Met.*, 1995, vol. 8(1), pp. 1–5. https://doi.org/10.1080/09534962.1995.11819186.
36. S. Vazehrad, J. Elfsberg, and A. Diószegi: *Mater. Charact.*, 2015, vol. 104, pp. 132–38. https://doi.org/10.1016/j.matchar.2014.09.008.
37. V. Fourlakidis, R. Lora, and A. Diószegi: *Mater. Sci. Forum*, 2014, vol. 790–791, pp. 211–16. https://doi.org/10.4028/www.scientific.net/MSF.790-791.211.
38. K.R. Olen and R.W. Heine: *Cast Met Res. J.*, 1968, vol. 4(1), pp. 28–43.
39. R.W. Heine and C.R. Loper: *AFS Trans.*, 1969, vol. 77, pp. 185–91.
40. B. Domeij, J.C. Hernando, and A. Diószegi: *Metall. Mater. Trans. B*, 2018, vol. 49(5), pp. 2487–2504. https://doi.org/10.1007/s11663-018-1274-z.
41. K. Lakeland and L. Hogan: *Iron and Steel Inst. Publ.*, 1968, vol. 45, pp. 213–23.
42. H. Fredriksson: *Metall. Trans. A*, 1975, vol. 6A, pp. 1658–660. https://doi.org/10.1007/BF02641981.
43. W. Kurz and D. Fisher: *Int. Met. Rev.*, 1979, vol. 24(1), pp. 177–204. https://doi.org/10.1179/imtr.1979.24.1.177.
44. H. Jones and W. Kurz: *Metall. Trans. A*, 1980, vol. 11(8), pp. 1265–73. https://doi.org/10.1007/BF02653480.
45. A. Diószegi, V. Fourlakidis, and R. Lora: *Int. J. Cast Met. Res.*, 2015, vol. 28(5), pp. 310–17. https://doi.org/10.1179/1743133615Y.0000000018.
46. J.C. Hernando and A. Diószegi: *Mater. Sci. Forum*, 2018, vol. 925, pp. 90–97. https://doi.org/10.4028/www.scientific.net/MSF.925.90.
47. J.C. Hernando, A. Diószegi, I.M. Agudo Medina, *7th International Conference on Solidification and Gravity*, 2018, pp. 238–243.
48. J.C. Hernando, B. Domeij, D. González, J.M. Amieva, and A. Diószegi: *Metall. Mater. Trans. A*, 2017, vol. 48(11), pp. 5432–41. https://doi.org/10.1007/s11661-017-4315-3.
49. A. Hultgren, Y. Lindblom, and E. Rudberg: *J. Iron Steel Inst.*, 1954, vol. 176, pp. 365–74.
50. W. Oldfield: *J. Br. Cast Iron Res. Assoc.*, 1960, vol. 8(2), pp. 177–92.
51. C.R. Loper and R.W. Heine: *AFS Trans.*, 1962, vol. 69, pp. 583–600.
52. J.-D. Schöbel: *Recent Res. Cast Iron*, 1964, vol. 20, pp. 303–46.
53. S.-E. Wetterfall, H. Fredriksson, and M. Hillert: *J. Iron Steel Inst.*, 1972, vol. 210(5), pp. 323–33.
54. T. Owadano, K. Yamada, and K. Torigoe: *Trans. Jpn Inst. Met.*, 1977, vol. 18(12), pp. 871–78. https://doi.org/10.2320/matertrans1960.18.871.
55. E.N. Pan, K. Ogi, and C.R. Loper Jr.: *AFS Trans.*, 1982, vol. 90, pp. 509–27.
56. N. Kayama, K. Nashimoto, K. Suzuki, *Report of the Castings Research Laboratory*, Waseda University, 1984, pp. 15–24.
57. J.C. Hernando and A. Diószegi: *Adv. Sci. Eng. Cast. Solidif.*, 2015, vol. 2, pp. 295–302. https://doi.org/10.1007/978-3-319-48117-3_35.
58. B. Domeij, J.C. Hernando, and A. Diószegi: *Metallogr. Microstruct. Anal.*, 2016, vol. 5(1), pp. 28–42. https://doi.org/10.1007/s13632-015-0250-0.
59. Z. Kulpa: *Comput. Graph. Image Proc.*, 1977, vol. 6(5), pp. 434–51. https://doi.org/10.1016/S0146-664X(77)80021-X.
60. E.E. Underwood: *J. Microsc.*, 1969, vol. 89(2), pp. 161–80. https://doi.org/10.1111/j.1365-2818.1969.tb00663.x.
61. D.G. Horvitz and D.J. Thompson: *J. Am. Stat. Assoc.*, 1952, vol. 47(260), pp. 663–85. https://doi.org/10.1080/01621459.1952.10483446.
62. F. Mampaey: *AFS Trans.*, 2000, vol. 27, pp. 11–17.
63. E.N.D. Souza, N. Cheung, and A. Garcia: *J. Alloys Compds.*, 2005, vol. 399(1), pp. 110–17. https://doi.org/10.1016/j.jallcom.2005.03.014.
64. P.W. Peterson, T. Kattamis, and A. Giamei: *Metall. Trans. A*, 1980, vol. 11(6), pp. 1059–65. https://doi.org/10.1007/BF02654720.